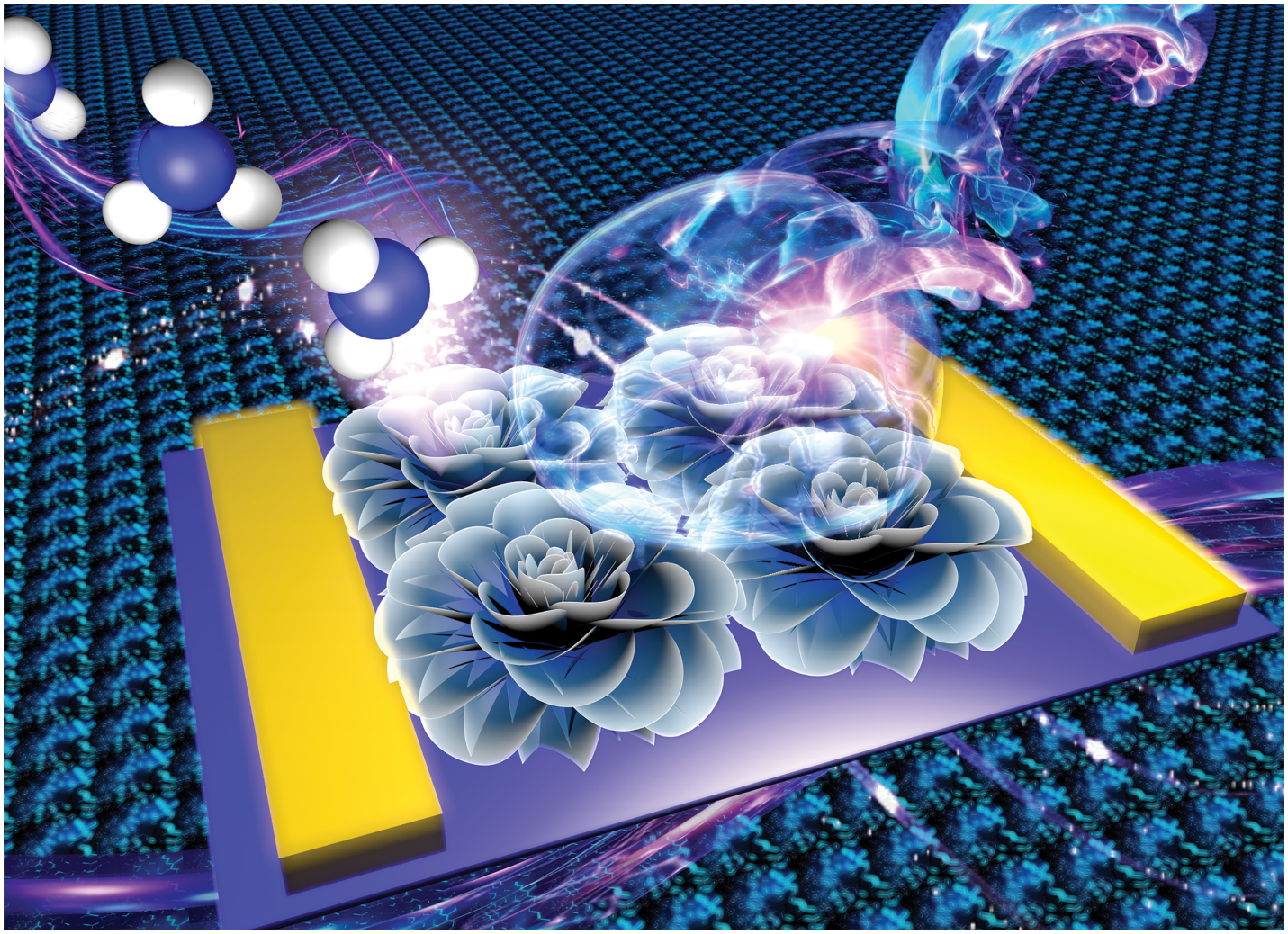

Showcasing research from Professor Hemen Kalita's laboratory, Department of Physics, Gauhati University, Assam, India.

Highly selective ammonia sensing at room temperature using DC plasma-modified MoS_2 nanoflowers

This cover art features the research work of Anurag Kashyap and Hemen Kalita from the Nanomaterials and Nanoelectronics Laboratory, Department of Physics, Gauhati University, Assam, India. It visually represents the enhancement in ammonia sensing by DC plasma-modified MoS_2 nanoflowers at room temperature. It highlights the effect of plasma treatment on the hydrothermally synthesized MoS_2 nanoflowers in enhancing sensitivity and selectivity towards very low concentrations of NH_3. This advancement holds potential for the development of efficient, low-cost gas sensors for environmental monitoring applications.

Image reproduced by permission of Anurag Kashyap and Hemen Kalita from *Mater. Adv.*, 2025, **6**, 3828.

As featured in:

See A. Kashyap, Hemen Kalita *et al.*, *Mater. Adv.*, 2025, **6**, 3828.

ROYAL SOCIETY OF CHEMISTRY

rsc.li/materials-advances

Registered charity number: 207890

Materials Advances

ROYAL SOCIETY OF CHEMISTRY

PAPER

View Article Online
View Journal | View Issue

Cite this: *Mater. Adv.*, 2025, 6, 3828

Highly selective ammonia sensing at room temperature using DC plasma-modified MoS_2 nanoflowers†

Anurag Kashyap, [a] Bipradip Chakraborty,[b] Tonmoi Hazarika,[c] Sanjeeb Chouhan, [a] Bharat Kakati [c] and Hemen Kalita *[a]

Received 14th March 2025,
Accepted 25th April 2025

DOI: 10.1039/d5ma00232j

rsc.li/materials-advances

This study explored the enhancement of ammonia (NH_3) sensing properties of MoS_2 nanoflowers through a direct current (DC) plasma treatment with nitrogen incorporation. Plasma treatment induced sulfur vacancies and introduced nitrogen atoms into the MoS_2 surfaces, enhancing the number of active sites and improving the charge carrier mobility. The structural and chemical alterations were confirmed by characterisations using FE-SEM, XPS, and Raman spectroscopy. The resulting plasma-treated MoS_2 sensor demonstrated highly selective detection of NH_3 at room temperature with a rapid response time of 22 s and a recovery time of 23 s. The experimental limit of detection was achieved at 5 ppm (theoretically ≈ 80 ppb), which was lower than the safety threshold set by the National Institute for Occupational Safety and Health (NIOSH). Results of DFT studies also agreed with the experimental results. Thus, this work highlights DC plasma treatment as an efficient, cost-effective approach to enhance gas sensing performance, with implications for developing highly sensitive and selective sensors for environmental monitoring and safety applications.

1. Introduction

In recent years, the detection of toxic gases has gained increasing importance in various fields, ranging from air quality control and workplace safety to medical diagnostics.[1–3] In particular, detection of ammonia (NH_3) has received significant interest owing to its adverse health effects, including severe respiratory conditions like asthma, emphysema, and chronic bronchitis, even when exposed to low levels.[4] Different types of sensing technologies, such as electrochemical cells and metal oxide chemiresistors, have been reported for the commercial detection of toxic gases.[5] However, these sensors often face challenges, such as the need for high operating temperatures and poor selectivity for differentiating between various gases.

To address these limitations, researchers have focused on alternative materials, particularly low-dimensional materials. Owing to their unique physiochemical properties, such as large specific surface areas, distinct electrical properties, and ease of functionalisation, 2D materials have gained significant importance in gas sensing in recent years.[4,6,7] Among the 2D materials, transition metal dichalcogenides (TMDs) are promising candidates for fabricating highly sensitive gas and volatile organic compound (VOC) sensors.[8] These materials provide weak gas-molecule binding and efficient charge transfer, enabling gas detection at room temperature.[9,10] Among the TMDs, molybdenum disulfide (MoS_2) has sparked a lot of research interest as a prominent sensing material owing to its high surface-to-volume ratio, high surface activity and sensitivity, quick response time, and outstanding stability.[11–16] In fact, MoS_2 is more appealing than graphene-based gas sensors owing to its semiconducting nature and the appropriate, adjustable band gap energies.[17] Despite its potential, MoS_2 still suffers from selectivity issues owing to similar VOC adsorption energies, making it difficult to detect one gas without interference from the other.[18,19] To overcome this, advanced fabrication techniques have been implemented, including doping, intercalation, and the creation of heterostructures, enhancing the material's ability to target specific gases more effectively.[20–24]

Plasma treatment is a prevalent method to alter the inherent physical and chemical properties of TMDs for application in gas sensing, ion storage, and oxygen reduction and hydrogen evolution reactions.[5,25–28] RF plasma treatment is commonly

[a] *Nanomaterials and Nanoelectronics Laboratory, Department of Physics, Gauhati University, Guwahati – 781014, Assam, India. E-mail: hemenkalita@gauhati.ac.in; Tel: +91 9769511692*
[b] *Department of Applied Science, Gauhati University, Guwahati – 781014, Assam, India*
[c] *META Laboratory, Assam Science and Technology University, Guwahati – 781013, Assam, India*

† Electronic supplementary information (ESI) available. See DOI: https://doi.org/10.1039/d5ma00232j

employed to alter surfaces because of its ability to provide homogeneous treatments applicable to 2D, complicated, and 3D materials.[29] The direct current plasma (DC plasma) treatment is another method by which material sensing properties can be modified by incorporating surface defects.[30,31] The procedure involves high-energy ions and reactive plasma species that alter the surface morphology and electronic characteristics. The creation of defects such as vacancies, surface states, and dangling bonds results in such changes, which increase the surface area. These modifications increase the sensitivity of the ability to adsorb the analyte, facilitate charge transfer, and thus increase the sensitivity and selectivity of the sensor. Moreover, plasma treatment with DC offers an avenue to modify sensor surfaces because it is extremely adaptable, less expensive than RF plasma, and suitable for a variety of materials.[31] Plasma processing has recently demonstrated itself as a rapid, convenient, straightforward, and effective approach for modifying the surface chemical characteristics of materials, particularly for the treatment of 2D materials without solvent contamination.[32,33] The chemical properties of the plasma process gas are crucial for determining the reaction mechanisms involved in plasma surface modification. Various gases, including oxygen, argon, helium, nitrogen, ammonia, carbon dioxide, and water, are used as process gases in surface modification techniques using plasma.[34] This approach may produce additional edge sites and heteroatoms, enhancing their charge carrier mobility and catalytic and optoelectronic capabilities.[35,36] Among the many existing methodologies, nitrogen plasma treatment has recently been recognized as an excellent approach for achieving controlled nitrogen atom incorporation into TMDs.[5,28,34,37] Zhao *et al.* developed an N-doped MoS_2 nanosheet-based sensor with improved sensitivity to NO_2 at room temperature.[28] Initially, MoS_2 nanosheets were hydrothermally fabricated and N-doping was performed *via* nitrogen plasma to synthesize N-MoS_2 nanosheets. Nitrogen atoms were introduced using a plasma-assisted technique. The atoms were adsorbed on the surface and doped into the lattice defects of MoS_2. This modified the electronic properties, such as the reduction of the Fermi level and the narrowing of the band gap.[36] The structure increased the conductivity and sensitization with NO_2, thereby increasing the response and reducing the detection limit.

This study reported the effects of DC plasma treatment on the NH_3 sensitivity of the MoS_2 nanoflower structure. Plasma-treated MoS_2 shows selective detection of NH_3 at RT (25 °C), greatly improving its sensing performance. N-MoS_2 sensor has a faster response time of 22 s and takes 23 s to recover. Moreover, plasma treatment significantly stabilized the sensing response of the sensor. The experimental and theoretical limits of detection were 5 ppm and 80 ppb, respectively. An effective way of improving room temperature NH_3 detection is described in this study.

2. Experimental section

2.1. Materials

Sodium molybdate ($Na_2MoO_4{\cdot}2H_2O$), thioacetamide (CH_3CSNH_2), and oxalic acid ($H_2C_2O_4$) were obtained from Sisco Research Laboratories (SRL) and used as received. The plasma treatment was performed using a glow discharge plasma reactor to produce N_2 and Ar plasma. Fig. 1 shows a schematic of the experimental assembly. Deionised water (DIW) was used throughout the experiment.

2.2. Synthesis of MoS_2

A wet chemical route is followed to synthesize MoS_2 nanoflowers. In a typical reaction, 1 g of sodium molybdate and 1.2 g

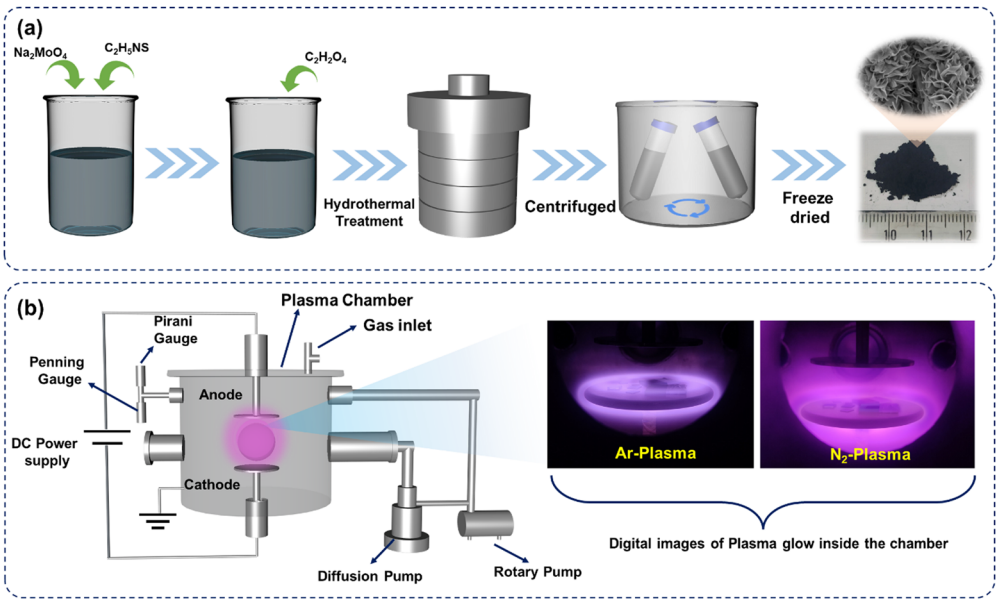

Fig. 1 Schematic of (a) synthesis of MoS_2 nanoflowers following the wet chemical route and (b) plasma treatment assembly with digital images of Ar and N_2 plasma during treatment.

of thioacetamide are stirred in 50 mL of DI water for 30 min at ambient temperature. Then, 0.6 g of oxalic acid was added to the mixture, which was further stirred for another 30 min. The solution was then hydrothermally treated for 24 h at 200 °C by being put in a 100 mL Teflon beaker and sealed inside a stainless steel (SS) container. After cooling to room temperature, the sample is centrifuged with ethanol and DI water and freeze-dried for 24 h.

2.3. Sensor electrode fabrication

Interdigitated electrode structures (IDE) have been fabricated following a standard copper (Cu) etching procedure using a ferric chloride ($FeCl_3$) solution. The desired IDE structure was transferred to the copper printed circuit board (PCB), which was dipped in $FeCl_3$ solution following agitation for the etching of the unwanted copper. Finally, the IDE structure remains on the board and is rinsed with ethanol and DI water and dried by purging nitrogen before deposition of the sensing material.

2.4. Synthesis of N-MoS_2

As nitrogen plasma is treated on the sensor, the sensor is termed as N-MoS_2 in the entire report. Sensors were treated with an argon/nitrogen plasma produced from a custom-built glow discharge reactor. The sensor was fabricated using the drop-casting method. The synthesized MoS_2 sample was dispersed and drop-cast on sensors composed of copper IDEs and dried in a vacuum oven at 60 °C for 3 h before plasma treatment. Fig. 1(b) shows a schematic of the experimental setup. The plasma chamber, a cylindrical stainless steel (SS 304L) vessel with a volume of approximately 3.5×10^3 cm^3 (diameter: 30.0 cm, height: 50.0 cm), was evacuated using a diffusion pump (1000 L min^{-1}) backed by a rotary pump (540 L s^{-1}). A base pressure of $\sim 10^{-6}$ mbar was achieved.

Two circular stainless steel (SS 304L) electrodes initiated the discharge and were powered by a DC power supply (1000 V, 2.5 A). Ultra-pure argon/nitrogen gas (99.99%) was introduced into the chamber through a digital flow controller to maintain a working pressure of 1.0×10^{-1} mbar. The sensors were exposed to Ar and N_2 plasma for 2 and 10 minutes, respectively.

A Langmuir probe was used for plasma diagnostics. The measured plasma density was 4.35×10^{15} m^{-3} and 4.43×10^{15} m^{-3} in the presence and absence of sensors, respectively. The electron temperature remained relatively constant at 1.38 eV. The slight decrease in plasma density observed in the presence of sensors is attributed to plasma-sample interactions.[34,38]

2.5. Computational details

The computations conducted utilised the density functional theory (DFT) – based Cambridge Serial Total Energy Package (CASTEP) module, which is integrated into the Materials Studio software suite.[4,7,39] The Kohn–Sham equations were solved using the plane-wave pseudopotential method developed within the DFT framework.[40] For the exchange–correlation function, the generalized gradient approximation (GGA), as outlined by Perdew–Burke–Ernzerhof (PBE), was used for geometry optimization.[41] Throughout the computations, the DFT-D dispersion correction suggested by Grimme and used in CASTEP was used to account for the van der Waals (vdW) intermolecular forces.[42] A $6 \times 6 \times 1$ k-point mesh was used to sample the Brillouin zone with an energy cutoff of 517 eV. Geometry optimization, which is essential for achieving a configuration's equilibrium state with minimum energy, was performed using the Broyden–Fletcher–Goldfarb–Shanno (BFGS) algorithm, which is highly effective for energy minimization in crystalline materials.[43]

A medium convergence tolerance was adopted for geometry optimization, and electronic minimization parameters utilized the Gaussian smearing scheme with a smearing width of 0.1 eV. Additionally, a 20 Å vacuum was introduced perpendicular to the interface surface to eliminate interactions between the interfaces and their periodic images.

The difference in charge density between the MoS_2 system and the adsorbed gas is computed as:

$$\Delta\rho = \rho_{(MoS_2+gas\_molecule)} - \rho_{gas\_molecule} \quad (1)$$

where $\rho_{(MoS_2+gas\_molecule)}$ and $\rho_{gas\_molecule}$ are the charge densities of the MoS_2 + gas molecule system and the gas molecule, respectively.

The binding energy of the adsorbed gas molecules is calculated using the equation:

$$E_b = E_{(MoS_2+gas\_molecule)} - E_{(gas_{molecule})} \quad (2)$$

where $E_{(MoS_2+gas\_molecule)}$ and $E_{(gas_{molecule})}$ are the total energies of the MoS_2 + gas molecule system and the gas molecule, respectively.

2.6. Characterization

The morphology of the synthesized samples were observed using field emission-scanning electron microscope (FE-SEM, ΣIGMA 300 VP, Carl Zeiss). The structural characteristics of the fabricated samples were characterized using an X-ray diffractometer (XPERT PRO, Philips/PANalytical) with Cu Kα radiation (1.54 Å) and with a laser micro-Raman system (Make: Horiba JobinYvon, Model: LabRam HR). XPS analyses were performed using an X-ray Photo Spectrometer (Model-K Alpha, Make: Thermo Fisher Scientific).

3. Results and discussions

3.1. Structural and morphological characterizations of MoS_2 and N-MoS_2

Fig. 2 shows the FESEM images and EDX analysis of MoS_2 and N-MoS_2. As shown in Fig. 2(a), the MoS_2 nanosheets are arranged in a flower-like structure. EDX analysis (Fig. 2(c)) provides elemental information about the synthesized materials. In the case of N-MoS_2 (Fig. 2(b)), the flower-like structure is intact with a bit of deformation, which may be due to the bombardment of energetic ions during argon plasma treatment, followed by nitrogen plasma. The EDX spectrum (Fig. 2(d)) shows the presence of nitrogen, which is absent in

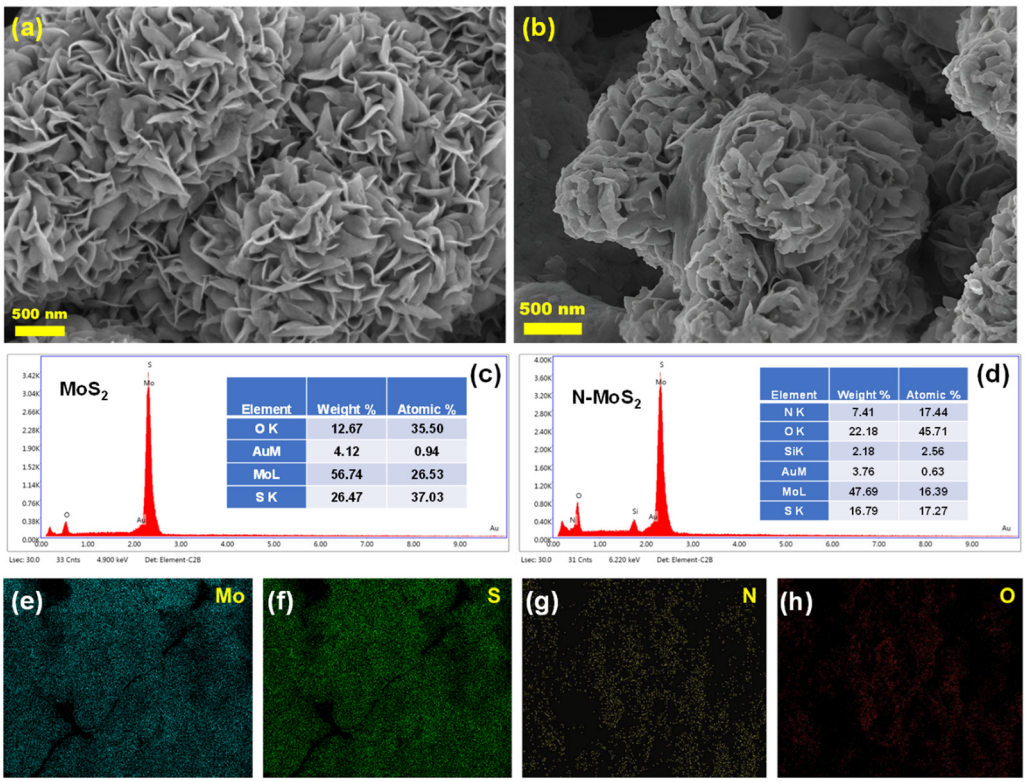

Fig. 2 FESEM images of (a) MoS_2 nanosheet and (b) N-MoS_2 nanosheet; EDX spectra of (c) MoS_2 and (d) N-MoS_2; and (e)–(h) colour mapped images of Mo, S, N and O elements of N-MoS_2 sample.

the EDX spectrum of MoS_2 (Fig. 2(c)). The colour-mapping images of different elements present in the nitrogen-incorporated MoS_2 sample are shown in Fig. 2(e-h).

Fig. 3(a) shows the Raman spectra of MoS_2 and N-MoS_2, in which two distinct peaks E^1_{2g} and A^1_g represent the vibration modes of hexagonal MoS_2. The A^1_g peak that appears at $\sim$ 402 cm^{-1} is attributed to the out-of-plane vibration of Mo and S atoms, whereas E^1_{2g} appears at $\sim$375 cm^{-1} and is attributed to the in-plane vibration of Mo and S atoms.[44] The peak spacing between the E^1_{2g} and A^1_g peaks for both MoS_2 and N-MoS_2 was the same (26.4 cm^{-1}), confirming their similar layer numbers.[44] The Raman spectra of MoS_2 after various nitrogen plasma treatment times are presented in the ESI† (Fig. S1). The X-ray diffraction patterns of the synthesized MoS_2 nanoflowers and bulk MoS_2 are presented in the ESI† (Fig. S2). Fig. 3(b) shows the XPS survey spectra of MoS_2 and N-MoS_2. From this figure, the N/Mo ratios are 0.5 and 3.3 for MoS_2 and N-MoS_2, respectively. Fig. 3(c)–(h) shows the deconvoluted XPS spectra of the MoS_2 and N-MoS_2 samples. In Fig. 3(c), the Mo 3d spectrum of MoS_2 exhibits four peaks, among which Mo^{4+} $3d_{5/2}$ and Mo^{4+} $3d_{3/2}$ correspond to 228.9 eV and 232.0 eV, respectively.[45] Along with this, a small peak around 235 eV appears due to the oxidation of Mo on the MoS_2 surface and is assigned to Mo^{6+} $3d_{3/2}$ and Mo^{6+} $3d_{5/2}$, respectively.[46] The peak at 226.1 eV was assigned to the S 2s of MoS_2.[45] For N-MoS_2, the deconvoluted spectrum of Mo 3d in Fig. 3(f) shows the peak present at 233.5 eV along with the peaks present in Fig. 3(c), which arise due to bonds between Mo and N.[28,47,48] Moreover, the intensity of the Mo^{6+} 3d peaks increased, which may have been due to the oxidation of Mo after treatment.

Fig. 3(d) and (g) show the S 2p spectra of MoS_2 and N-MoS_2, respectively. Two peaks appear at 163.1 and 161.7 eV, corresponding to S^{2-} $2p_{1/2}$ and S^{2-} $2p_{3/2}$, respectively.[28] Fig. 3(e) and (h) show the Mo 3p spectra of MoS_2 and N-MoS_2, respectively. The peaks at 394.7 eV arise due to Mo $3p_{3/2}$ in both spectra. Along with that, two distinct and intense peaks in Fig. 3(h) at 398.5 eV and 402.0 eV appear due to characteristic Mo–N bond and N–O, respectively, which are less intense in the case of the Mo 3p deconvoluted spectrum of MoS_2 (Fig. 3(e)).[47,49]

3.2. Gas sensing measurements of the MoS_2 and N-MoS_2 sensors:

The gas sensing measurements of the MoS_2 and N-MoS_2 sensors were performed in a homemade sensing assembly (Fig. 4). The sensing material was dropcasted onto the inter-digitated electrode fabricated on the PCB, as described in Section 2.3. The sensor was then dried in a vacuum oven at 60 °C for 3 h. The sensor was then plasma-treated with argon and nitrogen plasma in a plasma chamber. The sensor was then exposed to VOCs in the gas sensing chamber (Fig. 4). The required amount of ammonia, calculated using the standard formula (ESI,† eqn (S1)), was inserted inside the sensing chamber.[4,7]

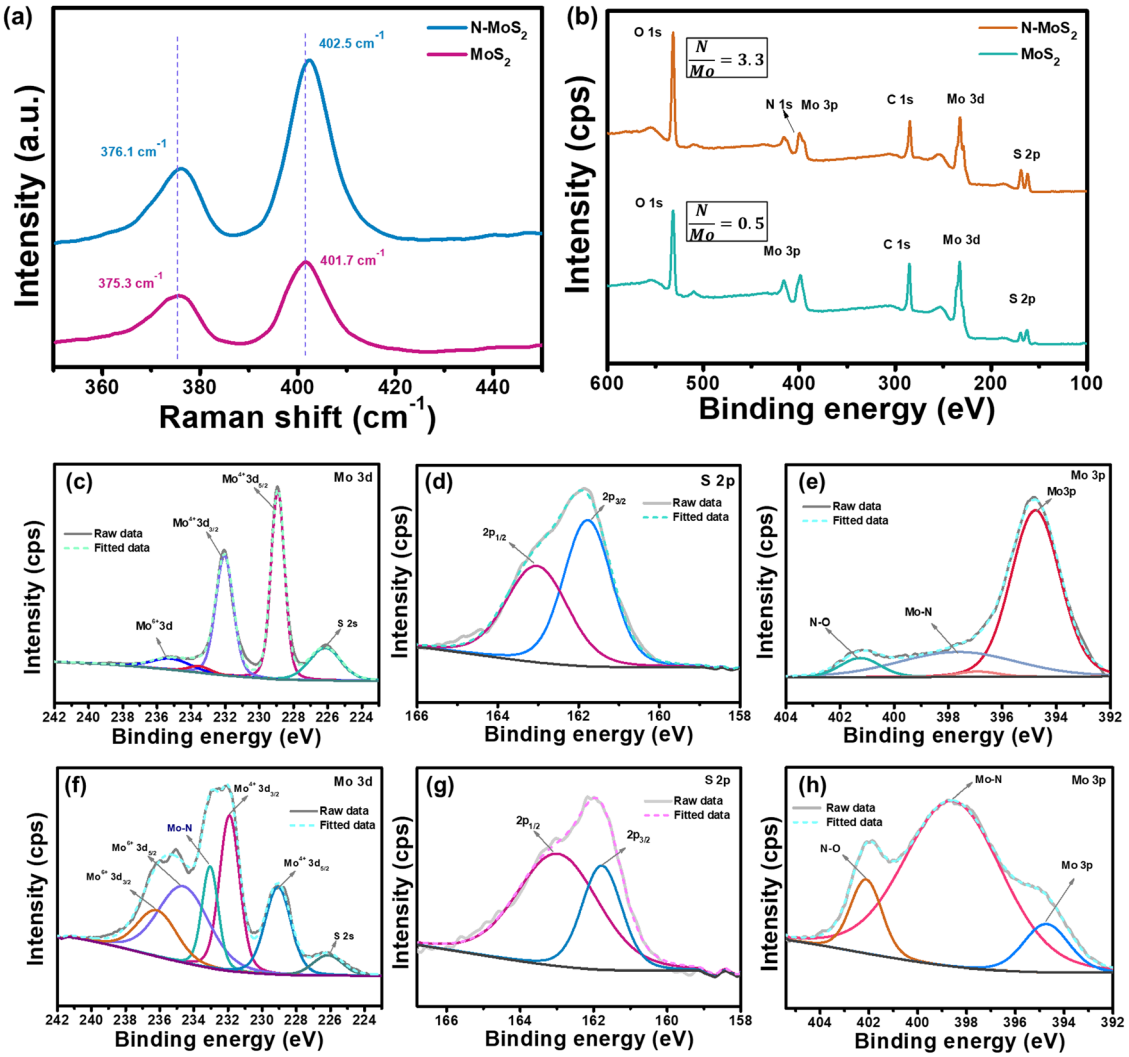

Fig. 3 (a) Raman spectra of MoS_2 and N-MoS_2 XPS; (b) XPS survey spectra of MoS_2 and N-MoS_2; XPS deconvoluted spectra of (c) Mo 3d, (d) S 2p, and (e) Mo 3p of the MoS_2 sample and (f) Mo 3d, (g) S 2p, and (h) Mo 3p of the N-MoS_2 sample.

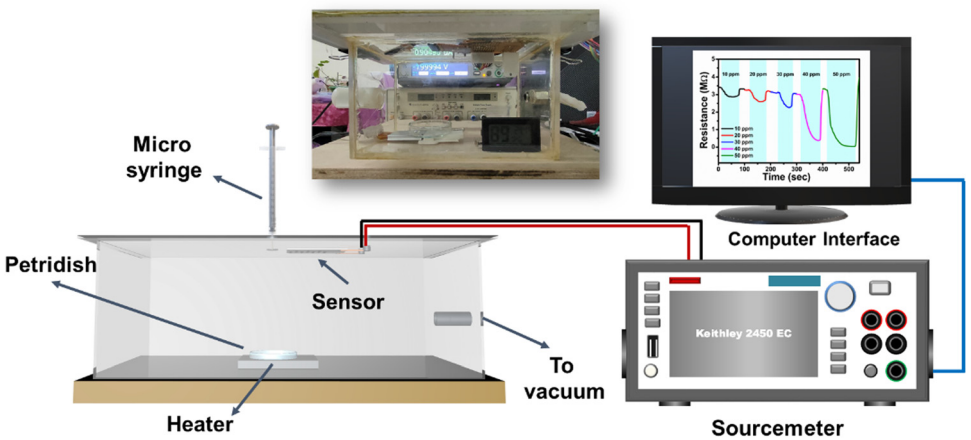

Fig. 4 Schematic of the gas sensing setup assembly; inset: digital image of the sensing assembly.

Fig. 5 shows the dynamic responses of the MoS_2 and N-MoS_2 sensors at room temperature towards ammonia (NH_3), formaldehyde (HCHO), and triethylamine (TEA). Fig. 5(a) shows the responses of the MoS_2 and N-MoS_2 sensors to ammonia. N-

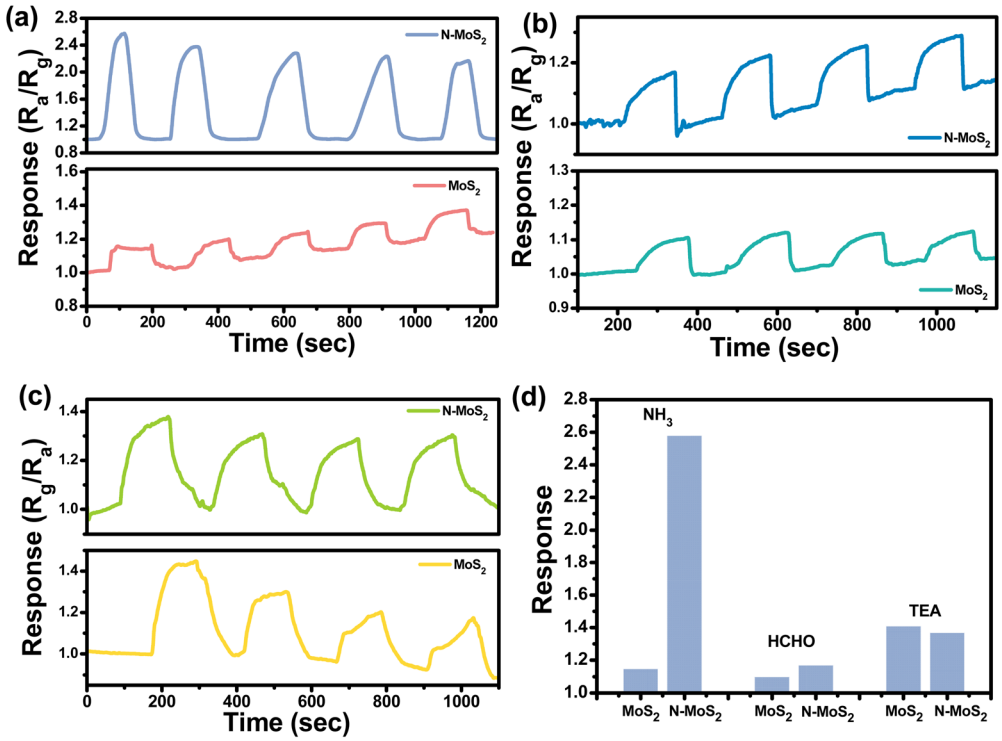

Fig. 5 Dynamic sensing responses of the MoS_2 and N-MoS_2 sensors towards (a) NH_3, (b) HCHO and (c) TEA at room temperature and (d) comparison of the sensing responses of MoS_2 and N-MoS_2 sensors towards various analyte VOCs.

MoS_2 sensor exhibits an enhanced sensing response to NH_3 compared to the MoS_2 sensor. In contrast, in the case of HCHO and TEA (Fig. 5(b) and (c)), there is little change in the response. Fig. 5(d) shows a comparison histogram of the sensing responses of MoS_2 and N-MoS_2 towards NH_3, HCHO and TEA, respectively. To check the selectivity of N-MoS_2 sensor towards common interfering VOCs, acetone and ethanol were also exposed to measure the sensing response.

The effect of plasma exposure time on the sensing performance of the MoS_2 nanoflower structure was analysed by exposing the nitrogen plasma at three different times (5 min, 10 min and 15 min). The sensing responses of the plasma-treated sensors and the non-treated MoS_2 sensor (MS sensor) are shown in Fig. 6. The different plasma-treated sensors were termed NMS_05 (5 min plasma exposure), NMS_10 (10 min plasma exposure), and NMS_15 (15 min plasma exposure), depending on the plasma exposure time. The results show that NMS_05 exhibits no significant change in response compared with the MS sensor. However, NMS_10 and NMS_15 sensors have similar responses to 10 ppm NH_3 vapour at room temperature.

Fig. 7(a) shows the selectivity of the synthesized N-MoS_2 sensor towards various VOCs. As shown in the figure, the sensor is highly selective towards NH_3 compared to other common VOCs in the ambient environment. Fig. 7(b) shows the response and recovery times of N-MoS_2 towards 10 ppm NH_3 vapour. The response time of a sensor is the time taken for the resistance to reach 90% of its total change when the sensor is in the proximity of the target gas, while the recovery time is the duration needed for the resistance to return to 90% of its original baseline after the gas is removed.[4,7] The response time of the sensor was 22 s, whereas the recovery time was 23 s.

The dynamic changes in the response of the sensor to 10 ppm NH_3 vapour are shown in Fig. 7(c). Up to five cycles, the sensor showed an almost constant response with a little bit of deviation from the initial response. Fig. 7(d) shows the variation in sensor resistance towards 10 ppm NH_3 vapour. The changes in the resistance values were almost constant from the baseline value, with a deviation at the initial cycle.

Fig. 8(a) shows the dynamic response of N-MoS_2 sensor to varying NH_3 concentrations during continuous measurement. The sensor has a very high response with increasing concentrations of the analyte vapour, which may be due to humidity. Fig. 8(b) shows the linear response with the fitting curve of N-MoS_2 sensor to different VOC concentrations. From the calibration curve with increasing concentration of the NH_3 vapour, it can be observed that the curve is statistically linear with a correlation coefficient value R^2 = 0.97. The theoretical estimation of the limit of detection (LOD) of the sensor can be estimated using the following eqn (3):[50]

$$\mathrm{LOD} = 3\frac{\mathrm{RMS_{noise}}}{\mathrm{Slope}} \quad (3)$$

where RMS_{noise} is estimated using the root mean square deviation from the variation of the relative sensor response in the baseline before exposing the sensor to the NH_3 vapour and the

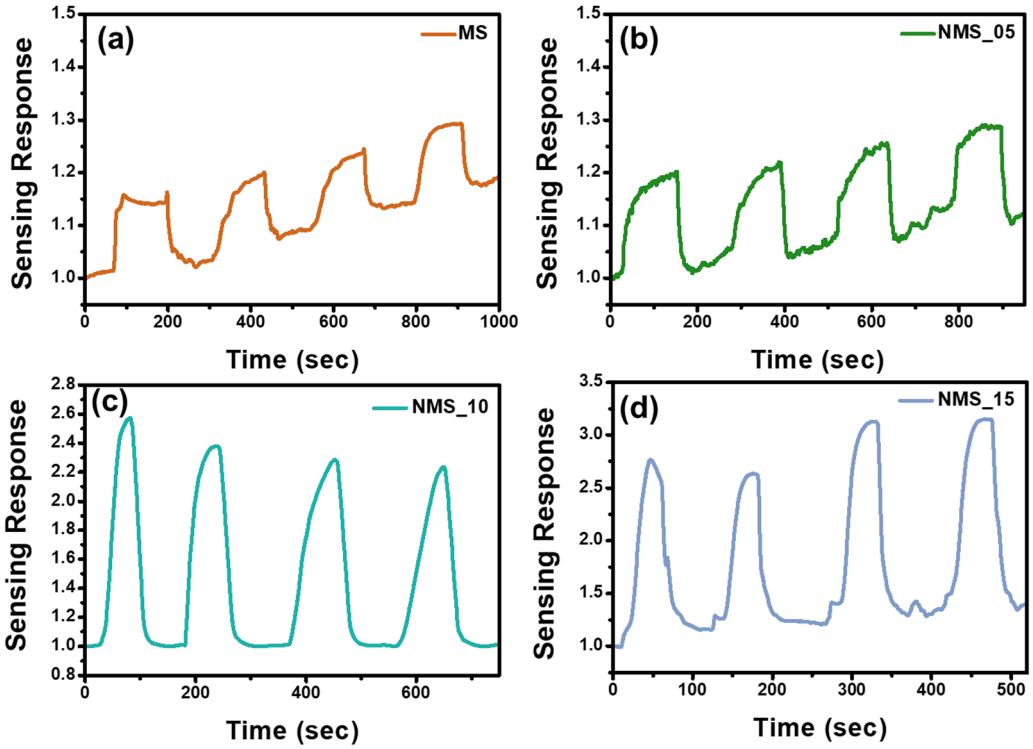

Fig. 6 Dynamic sensing response of (a) MoS_2 (MS sensor) and N-MoS_2 sensors with different nitrogen plasma exposure times of (b) 5 min (NMS_05), (c) 10 min (NMS_10), and (d) 15 min (NMS_15) towards 10 ppm NH_3 vapour.

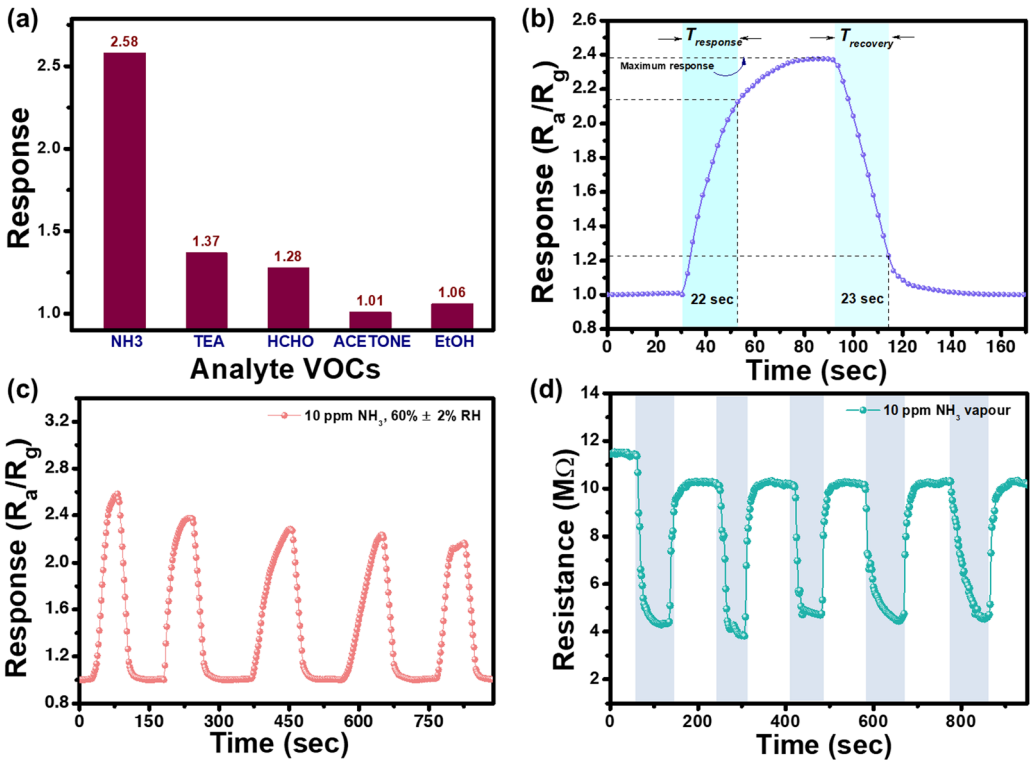

Fig. 7 (a) Selectivity of N-MoS_2 sensor towards different analyte VOCs; (b) response and recovery time measurements of N-MoS_2 sensor; (c) dynamic sensing response of N-MoS_2 sensor towards 10 ppm NH_3; and (d) resistance change during the exposure of 10 ppm NH_3 vapour to N-MoS_2 sensor.

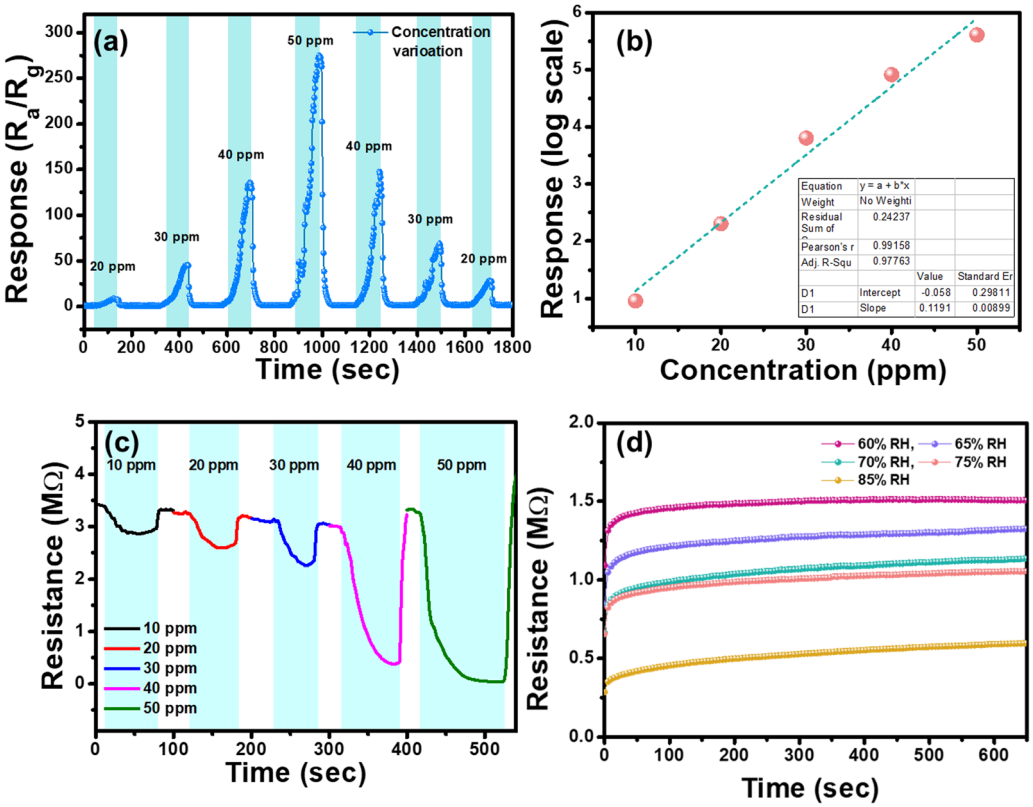

Fig. 8 (a) Response of N-MoS_2 sensor to varying concentrations of NH_3 in a continuous measurement; (b) linear response with fitting curve of N-MoS_2 sensor to different VOC concentrations; (c) measurement of resistance changes from its baseline resistance with increasing concentration of analyte VOC at room temperature; and (d) variation in the baseline resistance of the sensor with varying relative humidity.

slope refers to the slope of the linear fitting curve in Fig. 8(b). The slope was calculated as 0.1191. The RMS_{noise} is calculated using eqn (4):

$$RMS_{noise} = \sqrt{\frac{S^2}{N}} \quad (4)$$

where S is the standard deviation (S.D.) of the data before exposing the sensor to formaldehyde vapour and N is the corresponding data point. From Fig. 8(a), the standard deviation for $N = 80$ (the data before the sensor is exposed to NH_3 vapour) is ≈ 0.0284. Therefore, RMS_{noise} is 0.00319, and using eqn (3), the LOD is 0.080 ppm $\approx$ 80 ppb.

Fig. 8(c) shows the dynamic resistance changes of N-MoS_2 sensor with varying concentrations of NH_3 vapour. The sensor is sensitive to humidity, and with an increase in the analyte VOC's volume, the humidity inside the chamber also increases, which enhances the sensor's response to high concentrations of NH_3. Fig. 8(d) shows the variation in baseline resistance at different relative humidity values inside the sensing chamber at room temperature.

3.3. Computational analysis

For the computational analysis, a $4 \times 4 \times 1$ supercell of MoS_2 containing 48 atoms was used. In the equilibrium state, the Mo and S atoms of the MoS_2 monolayer form a hexagonal lattice. The lattice constants of the MoS_2 monolayer are $a = 3.21$ Å and $c = 12.14$ Å. The values are in good agreement with earlier experimental and theoretical results.[51] To depict the incorporation of nitrogen and sulphur vacancy in the MoS_2 monolayer, one sulphur atom was replaced by a nitrogen atom, and one sulphur atom was removed.

The optimised geometrical configurations of nitrogen-incorporated MoS_2 monolayers with sulfur vacancy and with different gases are presented in Fig. 8. All possible binding sites of the MoS_2 monolayer were considered, and the configuration with the highest binding energy was considered in further calculations to reflect the most probable experimental scenario.

The binding energies of all gases in the nitrogen-incorporated MoS_2 monolayer, as calculated using eqn (4), are shown in Fig. 9. The binding energy of the NH_3 molecule with the nitrogen-incorporated MoS_2 monolayer was the highest (−0.81 eV). The binding energy of the TEA molecule was the lowest (−0.18 eV). This finding is in close agreement with the sensing response of the nitrogen-incorporated MoS_2 monolayer. To delve deeper into the interaction between the various gases and the nitrogen-incorporated MoS_2 monolayer, a substantial charge transfer occurs between them, as shown in Fig. 9. In addition to the N-MoS_2 system with S vacancy, the effect of NH_3 adsorption on the N-MoS_2 system without S

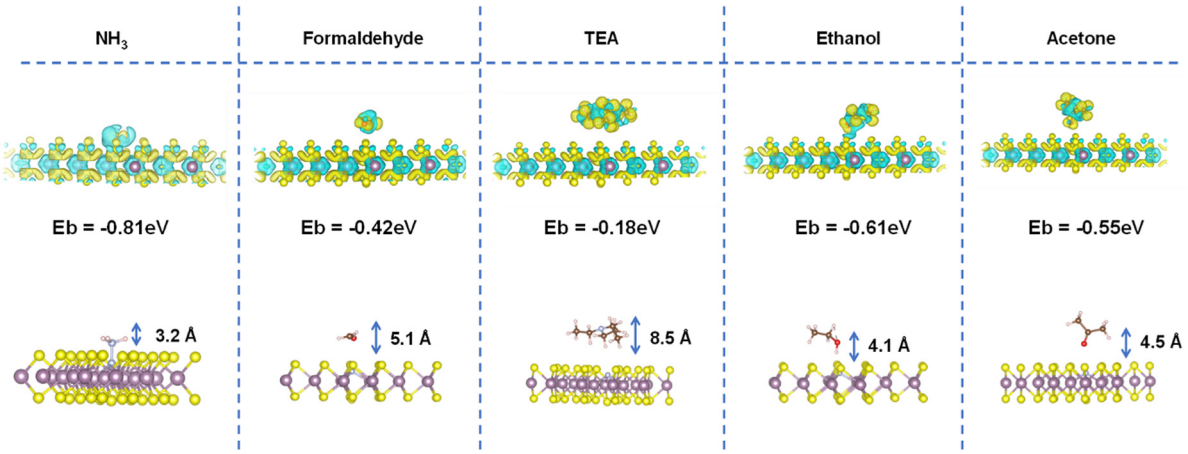

Fig. 9 Optimized configuration structures with electron charge density differences (EDDs) ($\Delta\rho$) of N-MoS_2 sample with S vacancy, along with intermolecular distances of N-MoS_2 with various VOCs. The yellow colour corresponds to charge accumulations, and the cyan colour corresponds to charge depletion.

vacancy was investigated. The charge density difference plots of all gases and the MoS_2 and nitrogen-incorporated MoS_2 monolayer without sulfur vacancies are shown in the ESI† (Fig. S3).

Similarly, from the intermolecular distances between gas molecules and nitrogen-incorporated MoS_2 monolayers with S vacancy, it was found that the NH_3 molecule exhibited the lowest distance (3.2 Å), whereas the TEA molecule exhibited the highest distance of 8.5 Å. This result can be explained by the increased electrostatic interaction between the NH_3 molecule and the nitrogen-incorporated MoS_2 monolayer.

For comparison, the binding energy values of all three systems (*i.e.*, only MoS_2, N-MoS_2 without S vacancy, and N-MoS_2 with S vacancy) are summarized in Tables 1, 2 and 3, respectively.

To examine the changes in the electronic properties of the nitrogen-incorporated MoS_2 monolayer upon NH_3 molecule adsorption, the total density of states (TDOS) was plotted (Fig. 10). The adsorption of the NH_3 molecule on the nitrogen-incorporated MoS_2 monolayer leads to a significant shift in the Fermi level towards higher energy. This also introduces new peaks at the conduction band at 0.52 eV and 1.97 eV. This shows that the introduction of the NH_3 molecule results in changes in the electronic properties of the nitrogen-incorporated MoS_2 monolayer.

To delve deeper into the mechanism behind the change in the density of the state of N-MoS_2 after NH_3 adsorption, we calculated the PDOS of N-MoS_2 with a sulphur vacancy before NH_3 adsorption and N-MoS_2 with a sulphur vacancy after NH_3 adsorption. From Fig. 11(a), it can be seen that the major contribution in the valence band near the Fermi level is from the d_z^2 orbital of molybdenum atoms, followed by a contribution from the p_z orbital of sulphur atoms. In contrast, in the case of N-MoS_2 with S vacancy after NH_3 adsorption, the major contribution in the conduction band near the Fermi level is from the $d_{x^2-y^2}$ orbital of Molybdenum atoms, followed by a contribution from the p_y orbital of sulphur atoms (Fig. 11(b)).

Table 1 Adsorption energy and intermolecular distances of pure MoS_2 monolayers

System	Adsorption energy (eV)	Intermolecular distance (Å)
MoS_2 + ammonia	−0.38	5.2
MoS_2 + formaldehyde	−0.31	5.1
MoS_2 + TEA	−0.18	9.4
MoS_2 + ethanol	−0.27	5.8
MoS_2 + acetone	−0.35	5.5

Table 2 Adsorption energy and intermolecular distances for nitrogen-incorporated MoS_2 monolayers (without sulphur vacancy)

System	Adsorption energy (eV)	Intermolecular distance (Å)
MoS_2 + ammonia	−0.76	3.9
MoS_2 + formaldehyde	−0.45	5.7
MoS_2 + TEA	−0.12	9.1
MoS_2 + ethanol	−0.53	4.7
MoS_2 + acetone	−0.42	5.2

Table 3 Adsorption energy and intermolecular distances of nitrogen-incorporated MoS_2 monolayers (with sulphur vacancy)

System	Adsorption energy (eV)	Intermolecular distance (Å)
MoS_2 + ammonia	−0.81	3.2
MoS_2 + formaldehyde	−0.42	5.1
MoS_2 + TEA	−0.18	8.5
MoS_2 + ethanol	−0.61	4.1
MoS_2 + acetone	−0.55	4.5

3.4. Gas sensing mechanism:

The sensing mechanism of N-MoS_2 sensor is based on the change in the electrical resistance during the interaction of analyte vapour and the sensing material. Argon plasma treatment before nitrogen plasma may create sulfur vacancy due to

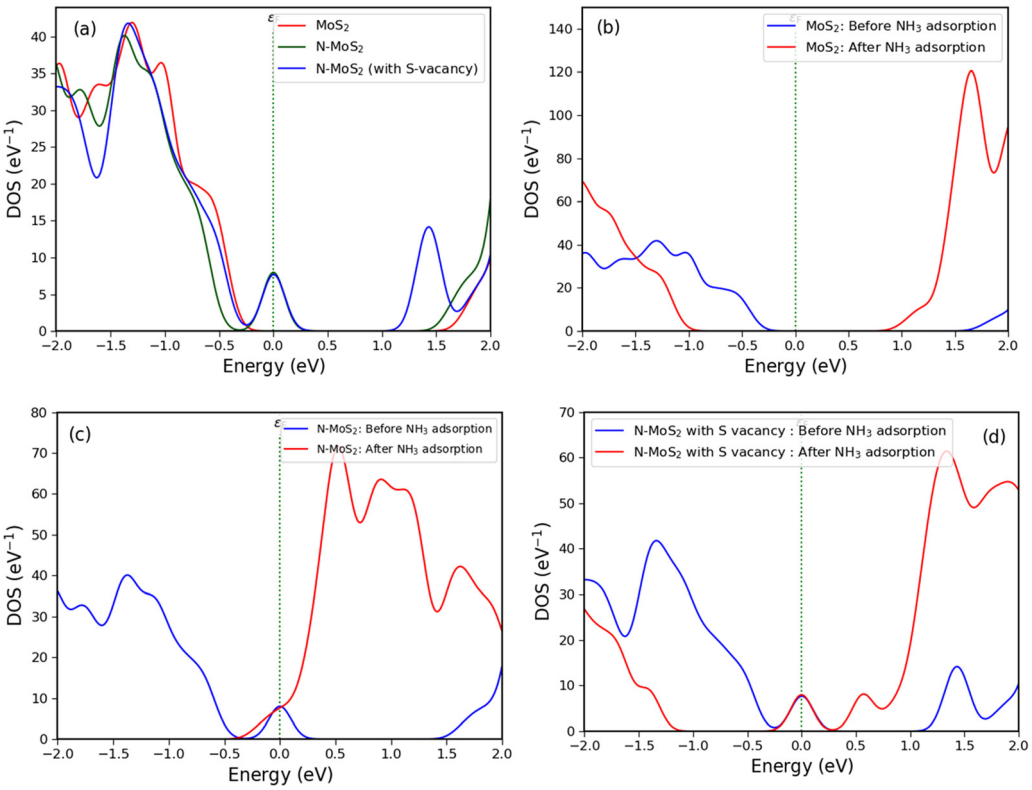

Fig. 10 Total density of state (TDOS) of the (a) MoS_2 system with N attachment and N attachment with S vacancy before NH_3 adsorption; (b) MoS_2 upon NH_3 molecule adsorption; (c) N-MoS_2 without sulfur vacancy upon NH_3 molecule adsorption; and (d) N-MoS_2 with S vacancy upon NH_3 molecule adsorption.

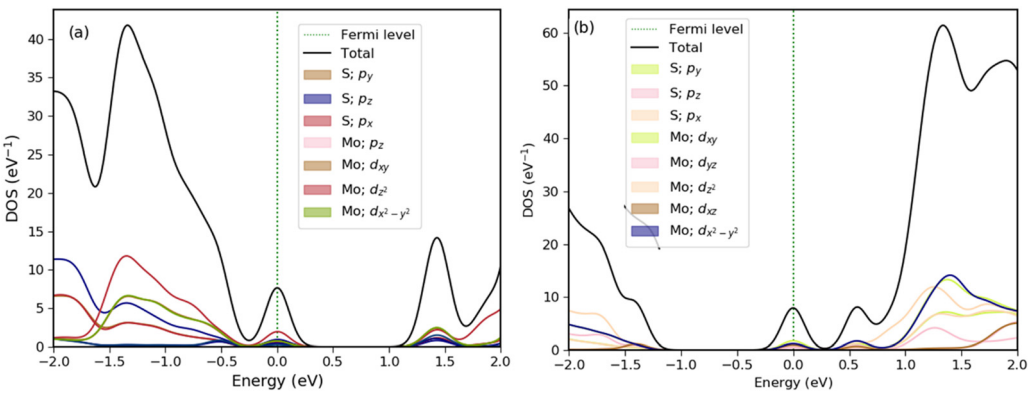

Fig. 11 Projected density of states (PDOS) of (a) N-MoS_2 with S vacancy: before NH_3 adsorption and (b) N-MoS_2 with S vacancy: after NH_3 adsorption.

the bombardment of energetic ions, contributing to the n-type characteristics of N-MoS_2.[52–54] Additionally, oxygen may get adsorbed on the sulfur vacancies, creating oxygen adsorbates, which may also contribute to the n-type behaviour of the sensor.[55,56] Along with this, nitrogen plasma treatment may attach nitrogen to the MoS_2, which enhances electron carrier concentration in MoS_2 by introducing donor levels adjacent to the conduction band, hence augmenting n-type conductivity.[57–59] Moreover, the incorporation of nitrogen can make the sensor exhibit a more stable response than a non-treated MoS_2 sensor.[60] Fig. 12 shows the plausible sensing mechanism of N-MoS_2 sensor towards NH_3 vapours.

The *I–V* characteristic plot (ESI,† Fig. S4) also shows an increase in current after plasma treatment, which is also an n-type behaviour of N-MoS_2 sensor. When the NH_3 molecules interact with the sensing material, electron transfer occurs from NH_3 to the sensing material, which changes the resistance of the sensing material.[4] Hence, plasma treatment can enhance the sensing capabilities of MoS_2 sensors. The theoretical investigations are also consistent with the experimental results.

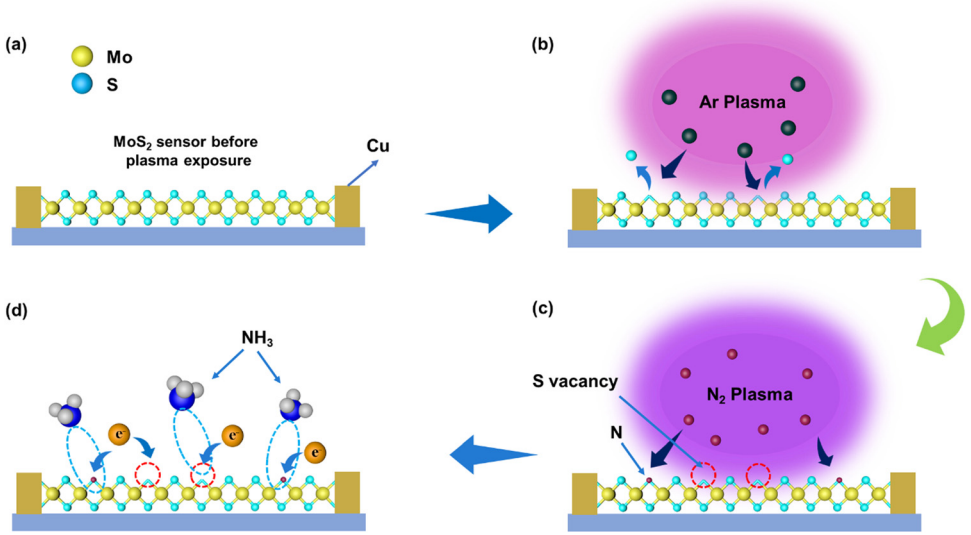

Fig. 12 (a) MoS_2 sensor before plasma treatment; (b) Ar plasma treatment on the MoS_2 sensor creating S vacancies; (c) N_2 plasma treatment on the sensor with nitrogen attachments taking place at some vacancies; and (d) interaction of NH_3 molecules with S vacancies and nitrogen attachment sites.

Table 4 Comparison of various MoS_2 sensors doped using plasma treatment and other chemical routes with this work

Sl no.	Title description	Targeted Gas/VOCs	Operating temperature	Limit of detection (LOD)	Response/recovery time	Ref.
1	Electronic modulation of MoS_2 nanosheets *via* N-doping	NO_2	Room temperature	62.5 ppb	53 s/323 s (10 ppm)	28
2	Synergetic phase modulation and N-doping of MoS_2	NO_2	Room temperature	0.13 ppm	43.1 s/301.2 s (10 ppm)	61
3	Metal-doped MoS_2 nanoflower	SO_2	Room temperature	250 ppb	—	62
4	Zinc-doped MoS_2/RGO composites	NH_3	200 °C	6 ppm	21.3 s/44.9 s (50 ppm)	63
5	N dopant-triggered MoS_2 nanosheets	NO_2	Room temperature	125 ppb	20 s/113 s (10 ppm)	37
6	Dual functionalized flower-like MoS_2 nanospheres with Pd and g-C_3N_4	TEA	225 °C	17 ppb	38 s/26 s (30 ppm)	64
7	N-doped MoS_2 hierarchical structures	NO_2	25 °C	10 ppb	146 s/52 s (10 ppb)	60
8	Cu-functionalized MoS_2 nanoworm thin films	NO_2	100 °C	2 ppm	54 s/82 s	65
9	Co-incorporated MoS_2 nanosheets	NO_2	Room temperature	7 ppm	10 s/600 s	18
10	**DC Plasma-modified MoS_2 nanoflower**	**NH_3**	**Room temperature**	**80 ppb**	**22 s/23 s**	**This Work**

Table 4 presents a comparison among various MoS_2-based sensors modified by plasma treatment, as well as doping by chemical methods, with the work presented here.

4. Conclusion

In summary, we fabricated a nitrogen-incorporated MoS_2 sensor following DC plasma treatment with a highly selective sensing response towards NH_3 at room temperature. MoS_2 was synthesized following a wet chemical approach following argon and nitrogen plasma treatment, which created sulfur vacancies and nitrogen incorporation into the MoS_2 matrix. The XPS spectra of the plasma-treated sensor showed an increase in nitrogen content compared with the non-treated sample. Moreover, the FESEM images also show some deformation after plasma treatment. EDX spectra also show nitrogen content. Plasma treatment enhances the number of active sites on the MoS_2 surface, which enhances the transfer of electrons from NH_3 to the active sites and increases the sensing response of the sensor compared to the pristine MoS_2 sensor. The sensor shows a fast response (22 s) and recovery time (23 s). The sensor also shows very selective detection of NH_3 compared to other common toxic VOCs, with a limit of detection of 80 ppb. This DC plasma treatment method can be applied for the fabrication of very highly sensitive VOC sensors in a controllable manner.

Author contributions

A. K. – conceptualization, methodology, investigation, formal analysis, visualization, data curation, and writing of the original draft. B. C. – methodology (theoretical), investigation, and writing – original draft. T. H. – methodology, investigation, data curation, and writing – original draft. S. C. – investigation, data curation. B. K. – resources, investigation, H. K. – resources, conceptualization, visualization, supervision, funding acquisition, and writing – review and editing*.

Data availability

The data supporting this article have been included as part of the ESI.†

Conflicts of interest

The authors declare no competing financial interest.

Acknowledgements

The authors are thankful to Sophisticated Analytical Instrument Facility (SAIF) and Central Instrument Facility (CIF), Gauhati University (GU), IIT Guwahati, and National Chemical Laboratory, Pune for providing material characterization facilities. H. K. would like to thank DST-PURSE (SR/PURSE/2022/116), ISRO (RAC-S, GU/RAC-S/01/2020-21/03), and Joint Network Centre: Indo-South Korea joint project (INT/Korea/JNC/CPS, DST, Govt. of India, 2021–2024) for providing the financial support. A. K. would like to thank CSIR-HRDG for providing fellowship under the SRF-Direct Scheme. B. C. would like to thank the Department of Applied Sciences, GU, for providing the computation facility for the simulation.

References

1 S. Freddi, A. V. Emelianov, I. I. Bobrinetskiy, G. Drera, S. Pagliara, D. S. Kopylova, M. Chiesa, G. Santini, N. Mores, U. Moscato, A. G. Nasibulin, P. Montuschi and L. Sangaletti, *Adv. Healthcare Mater.*, 2020, **9**, 2000377.
2 L. Zhang, K. Khan, J. Zou, H. Zhang and Y. Li, *Adv. Mater. Interfaces*, 2019, **6**, 1901329.
3 V. Van Tran, D. Park and Y. C. Lee, *Int. J. Environ. Res. Public Health*, 2020, **17**, 2927.
4 A. Kashyap, H. Sarma, B. Chakraborty and H. Kalita, *ACS Appl. Electron. Mater.*, 2024, **6**, 6916–6931.
5 K. Wang, L. Lee, S. L. Loo, T. Y. Yang, C. T. Chen, T. W. Kuo, J. L. Chen, H. C. Kuo and Y. L. Chueh, *ACS Appl. Nano Mater.*, 2023, **6**, 5336–5344.
6 W. C. Tan and K. W. Ang, *Adv. Electron. Mater.*, 2021, **7**, 1–21.
7 A. Kashyap, B. Chakraborty, M. S. Siddiqui, H. Tyagi and H. Kalita, *ACS Appl. Nano Mater.*, 2023, **6**, 7948–7959.
8 S. Acosta and M. Quintana, *Sensors*, 2024, **24**, 1817.
9 H. Schmidt, F. Giustiniano and G. Eda, *Chem. Soc. Rev.*, 2015, **44**, 7715–7736.
10 W. Zheng, X. Liu, J. Xie, G. Lu and J. Zhang, *Coord. Chem. Rev.*, 2021, **447**, 214151.
11 A. Shokri and N. Salami, *Sens. Actuators, B*, 2016, **236**, 378–385.
12 J. Chen and W. Xu, *eScience*, 2023, **3**, 100178.
13 P. Li, G. Zhang, Z. Kang, X. Zheng, Y. Xie, C. Liang, Y. Zhang, X. Fang, R. Sun, Z. Liu, Y. Bu, Y. Lu and Y. Zhang, *InfoMat*, 2023, **5**, e12457.
14 R. Duan, W. Qi, K. Tang and W. Liu, *InfoMat*, 2025, **7**, e12610.
15 J. Zhao, Z. Chen, S. Liu, P. Li, S. Yu, D. Ling and F. Li, *BMEMat*, 2024, **2**, e12066.
16 L. Luo, J. Gao, L. Zheng, L. Li, W. Li, M. Xu, H. Jiang, Y. Li, H. Wu, H. Ji, X. Dong, R. Zhao, Z. Liu, X. Wang and W. Huang, *InfoMat*, 2024, **6**, e12605.
17 L. Chacko, E. Massera and P. M. Aneesh, *J. Electrochem. Soc.*, 2020, **167**, 106506.
18 P. Bharathi, S. Harish, M. Shimomura, S. Ponnusamy, M. Krishna Mohan, J. Archana and M. Navaneethan, *Sens. Actuators, B*, 2022, **360**, 131600.
19 P. Bharathi, S. Harish, G. Mathankumar, M. Krishna Mohan, J. Archana, S. Kamalakannan, M. Prakash, M. Shimomura and M. Navaneethan, *Appl. Surf. Sci.*, 2022, **600**, 154086.
20 D. Zhang, Z. Yang, P. Li, M. Pang and Q. Xue, *Nano Energy*, 2019, **65**, 103974.
21 M. Ikram, L. Liu, H. Lv, Y. Liu, A. Ur Rehman, K. Kan, W. J. Zhang, L. He, Y. Wang, R. Wang and K. Shi, *J. Hazard. Mater.*, 2019, **363**, 335–345.
22 K. Rathi and K. Pal, *Adv. Mater. Interfaces*, 2020, **7**, 2000140.
23 Y. Liang, L. Zhang, K. Wang, J. Ren, L. Yu and M. Yin, *Sens. Actuators, B*, 2023, **378**, 133137.
24 J. Le Fan, X. F. Hu, W. W. Qin, M. Zhou, Y. S. Liu, S. Cheng, S. J. Gao, L. P. Tan, G. Q. Wang and W. Zhang, *J. Mater. Chem. C*, 2023, **11**, 2364–2374.
25 Z. Sheng, P. Qi, Y. Lu, G. Liu, M. Chen, X. Gan, Y. Qin, K. Hao and Y. Tang, *ACS Appl. Mater. Interfaces*, 2021, **13**, 34495–34506.
26 P. Tao, J. He, T. Shen, Y. Hao, J. Yan, Z. Huang, X. Xu, M. Li and Y. Chen, *Adv. Mater. Interfaces*, 2019, **6**, 1900460.
27 S. Deng, Y. Zhong, Y. Zeng, Y. Wang, Z. Yao, F. Yang, S. Lin, X. Wang, X. Lu, X. Xia, J. Tu, S. J. Deng, Y. Zhong, Z. J. Yao, X. L. Wang, X. H. Xia, J. P. Tu, Y. X. Zeng, X. H. Lu, Y. D. Wang, F. Yang and S. W. Lin, *Adv. Mater.*, 2017, **29**, 1700748.
28 K. Zhao, X. Chang, J. Zhang, F. Yuan and X. Liu, *ACS Sens.*, 2024, **9**, 388–397.
29 A. E. Abusrafa, S. Habib, I. Krupa, M. Ouederni and A. Popelka, *Coatings*, 2019, **9**, 145.
30 C. Ma, A. Nikiforov, D. Hegemann, N. De Geyter, R. Morent and K. Ostrikov, *Int. Mater. Rev.*, 2023, **68**, 82–119.
31 R. V. Dabhade, D. S. Bodas and S. A. Gangal, *Sens. Actuators, B*, 2004, **98**, 37–40.
32 S. Dou, L. Tao, R. Wang, S. El Hankari, R. Chen and S. Wang, *Adv. Mater.*, 2018, **30**, 1705850.
33 X. Ji, X. Yuan, J. Wu, L. Yu, H. Guo, H. Wang, H. Zhang, D. Yu and Y. Zhao, *ACS Appl. Mater. Interfaces*, 2017, **9**, 24616–24624.
34 T. Hazarika, B. Kakati, D. Pal, R. Saikia, A. Rawal, M. K. Mahanta and S. Biswas, *Sci. Rep.*, 2024, **14**, 1–23.
35 L. Tao, X. Duan, C. Wang, X. Duan and S. Wang, *Chem. Commun.*, 2015, **51**, 7470–7473.
36 A. Azcatl, X. Qin, A. Prakash, C. Zhang, L. Cheng, Q. Wang, N. Lu, M. J. Kim, J. Kim, K. Cho, R. Addou, C. L. Hinkle, J. Appenzeller and R. M. Wallace, *Nano Lett.*, 2016, **16**, 5437–5443.
37 R. Wu, J. Hao, S. Zheng, Q. Sun, T. Wang, D. Zhang, H. Zhang, Y. Wang and X. Zhou, *Appl. Surf. Sci.*, 2022, **571**, 151162.

38 T. Hazarika, P. Das, J. Jose, B. Kakati, D. Pal, R. Saikia and M. K. Mahanta, *Polym. Adv. Technol.*, 2023, **34**, 2862–2878.
39 S. J. Clark, M. D. Segall, C. J. Pickard, P. J. Hasnip, M. I. J. Probert, K. Refson and M. C. Payne, *Z. Kristallogr.*, 2005, **220**, 567–570.
40 C. Yang, Z. Y. Zhao, H. T. Wei, X. Y. Deng and Q. J. Liu, *RSC Adv.*, 2021, **11**, 4276–4285.
41 J. P. Perdew, K. Burke and M. Ernzerhof, *Phys. Rev. Lett.*, 1996, **77**, 3865.
42 S. Grimme, *J. Comput. Chem.*, 2006, **27**, 1787–1799.
43 T. H. Fischer and J. Almlöf, *J. Phys. Chem.*, 1992, **96**, 9768–9774.
44 S. Y. Cho, H. J. Koh, H. W. Yoo, J. S. Kim and H. T. Jung, *ACS Sens.*, 2017, **2**, 183–189.
45 Z. Chen, D. Yin and M. Zhang, *Small*, 2018, **14**, 1703818.
46 Y. Zhang, Y. Jiang, Z. Duan, Y. Wu, Q. Zhao, B. Liu, Q. Huang, Z. Yuan, X. Li and H. Tai, *J. Hazard. Mater.*, 2022, **434**, 128836.
47 L. Feng, L. Zhang, S. Zhang, X. Chen, P. Li, Y. Gao, S. Xie, A. Zhang and H. Wang, *ACS Appl. Mater. Interfaces*, 2020, **12**, 17547–17556.
48 F. Y. Meng, H. Wu, M. Qiao, X. F. Zeng, D. Wang and J. X. Wang, *Langmuir*, 2022, **38**, 1567–1577.
49 L. Lin, Z. K. Yang, Y. F. Jiang and A. W. Xu, *ACS Catal.*, 2016, **6**, 4449–4454.
50 D. Liu, J. Pan, J. Tang, W. Liu, S. Bai and R. Luo, *J. Phys. Chem. Solids*, 2019, **124**, 36–43.
51 E. S. Kadantsev and P. Hawrylak, *Solid State Commun.*, 2012, **152**, 909–913.
52 J. He, Y. Wen, D. Han, P. Zeng, P. Zheng, L. Zheng, W. Su, Z. Wu and Y. Zhang, *Mater. Sci. Semicond. Process.*, 2023, **158**, 107347.
53 K. Cho, M. Min, T. Y. Kim, H. Jeong, J. Pak, J. K. Kim, J. Jang, S. J. Yun, Y. H. Lee, W. K. Hong and T. Lee, *ACS Nano*, 2015, **9**, 8044–8053.
54 H. Qiu, T. Xu, Z. Wang, W. Ren, H. Nan, Z. Ni, Q. Chen, S. Yuan, F. Miao, F. Song, G. Long, Y. Shi, L. Sun, J. Wang and X. Wang, *Nat. Commun.*, 2013, **4**, 1–6.
55 A. Wu, Q. Song and H. Liu, *Comput. Theor. Chem.*, 2020, **1187**, 112906.
56 G. Sun, F. Li, T. Wu, L. Cong, L. Sun, G. Yang, H. Xie, A. Mauger, C. M. Julien and J. Liu, *Inorg. Chem.*, 2019, **58**, 2169–2176.
57 A. A. Kotsun, V. A. Alekseev, S. G. Stolyarova, A. A. Makarova, M. A. Grebenkina, A. P. Zubareva, A. V. Okotrub and L. G. Bulusheva, *J. Alloys Compd.*, 2023, **947**, 169689.
58 Q. Yang, Z. Wang, L. Dong, W. Zhao, Y. Jin, L. Fang, B. Hu and M. Dong, *J. Phys. Chem. C*, 2019, **123**, 10917–10925.
59 M. W. Jung, W. Song, D. S. Jung, S. S. Lee, C. Y. Park and K. S. An, *J. Nanosci. Nanotechnol.*, 2016, **16**, 2756–2759.
60 M. Yin, K. Wang, C. Gao, R. Yang, Y. Huang and L. Yu, *Mater. Res. Bull.*, 2024, **179**, 112943.
61 J. Kim, M. Li, C. H. Lin, L. Hu, T. Wan, A. Saeed, P. Guan, Z. Feng, T. Kumeria, J. Tang, D. Su, T. Wu and D. Chu, *Adv. Sci.*, 2025, **12**, 2410825.
62 D. Zhang, J. Wu, P. Li and Y. Cao, *J. Mater. Chem. A*, 2017, **5**, 20666–20677.
63 S. P. Linto Sibi, M. Rajkumar, K. Govindharaj, J. Mobika, V. Nithya Priya and R. T. Rajendra Kumar, *Anal. Chim. Acta*, 2023, **1248**, 340932.
64 W. Guo, K. Chen, S. Wang, H. Zhang and D. Wu, *Sens. Actuators, B*, 2025, **433**, 137490.
65 S. Tyagi, A. Kumar, A. Kumar, Y. K. Gautam, V. Kumar, Y. Kumar and B. P. Singh, *Mater. Res. Bull.*, 2022, **150**, 111784.